Available online at www.sciencedirect.com
SCIENCE DIRECT
ELSEVIER
Journal of Crystal Growth 290 (2006) 674–682
JOURNAL OF CRYSTAL GROWTH
www.elsevier.com/locate/jcrysgro

Study of the hydrodynamic instabilities in a differentially heated horizontal circular cylinder corresponding to a Bridgman growth configuration

S. Vaux, H. Ben Hadid, D. Henry*

Laboratoire de Mécanique des Fluides et d'Acoustique, UMR CNRS 5509, Ecole Centrale de Lyon/Université Claude Bernard Lyon 1/INSA de Lyon, ECL, 36 Av. Guy de Collongue, 69134 Ecully Cedex, France

Received 15 October 2004; received in revised form 31 December 2005; accepted 6 February 2006

Communicated by D.T.J. Hurle

Abstract

We are interested in determining the origin of the instabilities occurring in a metallic liquid (Prandtl number $Pr = 0.026$) contained in horizontal circular cylinders heated from the end-walls. Our approach by direct numerical simulation (DNS) allows the determination of the transition thresholds for different aspect ratios varying from 1.5 to 10 as well as a precise characterization of the nature and structure of the new flow regimes close to the thresholds. In order to understand the mechanisms of flow transition, fluctuating energy analyses close to the threshold have been performed. The main contributions have been determined and localized in the cavity: shear has been found as the main instability factor but the way it acts is different according to the aspect ratio.

PACS: 47.20.Bp

Keywords: A1. Computer simulation; A1. Convection; A1. Flow stability

1. Introduction

The control of the hydrodynamic instabilities occurring in the melt is crucial in material processing technologies such as crystal growth in order to optimize the quality of the elaborated crystals. In a differentially heated horizontal cylinder typical of horizontal Bridgman growth, convection always exists, but above a critical temperature difference between the endwalls of the cavity, the flow changes from a stationary to an oscillatory behavior. This transition could affect the quality of the grown crystal. Experimental studies have been carried out to identify the conditions for the appearance of such oscillations [1–4]. In simplified configurations, namely infinitely extended horizontal layer, thresholds have been calculated by theoretical approaches [5–7], but only few results are available in more realistic confined three-dimensional situations [8–10]. The more recent work concerning the oscillatory thresholds in parallelepidedic cavities by Wakitani [10] shows the evolution of the critical Grashof number as a function of the Prandtl number ($Pr \leqslant 0.03$) and the transverse aspect ratio which was varied from 0.5 to 4. The critical curves are found to evolve strongly with both parameters.

The present work investigates natural convection of a liquid metal in horizontal circular cylinders with differentially heated endwalls. The three dimensionless parameters that characterize the system are the cylinder aspect ratio, $A = L/D$, where L is the length and D is the diameter of the cylinder, the Prandtl number $Pr = \nu/\kappa$ where ν is the kinematic viscosity of the fluid and κ is the thermal diffusivity, and the Grashof number $Gr = \alpha g \Delta T D^4/\nu^2 L$, where ΔT is the temperature difference, g is the gravity vector and α is the thermal expansion coefficient.

*Corresponding author.
E-mail addresses: samuel.vaux@ec-lyon.fr, vaux@torroja.dmt.upm.es (S. Vaux), daniel.henry@ec-lyon.fr (D. Henry).

0022-0248/$ - see front matter © 2006 Elsevier B.V. All rights reserved.
doi:10.1016/j.jcrysgro.2006.02.013

This study will be focused on the detection of the instabilities and the characterization of their nature and origin on a large range of aspect ratios varying from 1.5 to 10.

2. Mathematical model

We consider a container filled with an incompressible Newtonian fluid and submitted to a horizontal temperature gradient (Fig. 1). The two ends of the cylinder are assumed isothermal. One end is held at temperature T_h, which is greater than the temperature T_c of the other end, and the sidewalls are considered to be adiabatic. All the physical characteristics are taken as constant, except the density which varies linearly with the temperature in the buoyancy term, $\rho = \rho_0[1 - \alpha(T - T_0)]$ (Boussinesq approximation), where T_0 is the mean temperature ($T_0 = (T_h + T_c)/2$). The governing equations for the temperature T, the pressure p, and the velocity $\mathbf{u}$ are the Navier–Stokes equations coupled with the energy equation. By scaling length by the diameter D of the cylinder, time by D^2/ν, velocity by $\nu\sqrt{Gr}/D$ and by introducing the dimensionless temperature field $\theta = A(T - T_0)/(T_h - T_c)$, the equations can be written in their dimensionless form as

$$\nabla.\mathbf{u} = 0, \tag{1}$$

$$\frac{\partial \mathbf{u}}{\partial t} + \sqrt{Gr}(\mathbf{u}.\nabla)\mathbf{u} = -\nabla p + \nabla^2\mathbf{u} + \sqrt{Gr}\,\theta\mathbf{e}_y, \tag{2}$$

$$\frac{\partial \theta}{\partial t} + \sqrt{Gr}(\mathbf{u}.\nabla)\theta = \frac{1}{Pr}\nabla^2\theta. \tag{3}$$

$\mathbf{e}_y$ is the unit vector in the vertical y direction.

For the boundary conditions, the no-slip velocity boundary condition is prescribed at all the container walls, the temperature is fixed at the endwalls, and along the lateral wall, the normal heat flux is zero. The governing equations and the associated boundary conditions verify a reflection symmetry S_p with respect to the middle longitudinal vertical L_v-plane and the π-rotational symmetry S_a about the transverse horizontal center T_h-axis. The combination of these two symmetries also gives a symmetry S_c with respect to the center point O of the cavity. These symmetries are those of the primary steady flow. When increasing Gr, bifurcations to new steady or oscillatory flow states may break the symmetries.

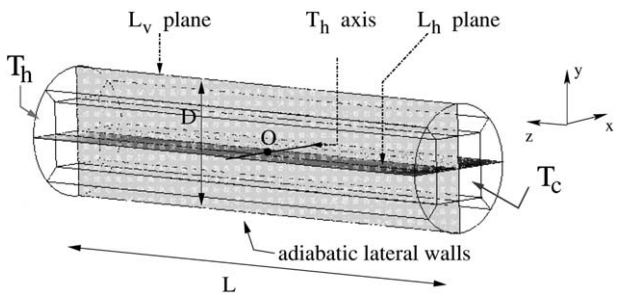

Fig. 1. Geometry of the cylindrical cavity and reference frame.

3. Numerical method

The equations of the problem are discretized in space with an isoparametric multidomain spectral elements method based on Gauss–Lobatto–Legendre (GLL) points distribution. The time discretization is based on a third-order mixed implicit–explicit time-splitting scheme using backwards differentiation [11]. The calculations were considered as converged if the difference between successive iterations scaled by the final values was less than or equal to 10^{-8}. For more details into the specifics of the technique, readers are referred to the paper of Touihri et al. [12] which details the procedures.

For this study, the cylindrical cavity is divided into 12 elements (Fig. 1) and the solution (u, v, w, p, θ) in the Cartesian coordinates (x, y, z) is represented in each element as a high-order Lagrangian interpolant through the standard GLL basis for all elements. Tests on the dependence of the results on both number of grid points and time-step have been performed. The optimal values of grid points and time stepping, i.e. those used for computations, which represent a good compromise between solution accuracy and computational time required, are assumed as those over which further refinements do not produce any noticeable modification in both the predicted flows and heat transfer rates. The accuracy of the results was then checked by calculating five quantities, which are the maximum of the velocity components $|u_{max}|$, $|v_{max}|$ and $|w_{max}|$, the Nusselt number, $Nu = (1/S)\int_{z=0}(\partial T/\partial z)\,dS$, and the total kinetic energy $K = \int_\Omega \frac{1}{2}\mathbf{u}^2\,d\Omega$. Different mesh sizes were used for different aspect ratios. In practice, we have taken $9 \times 9 \times nz$ points per element with nz varying from 27 for $A = 1.5$ to 61 for $A = 10$ (see details in Tables 1 and 2). The accuracy tests have shown that a refinement in the (xy)-cross section from $7 \times 7 \times nz$ points to $9 \times 9 \times nz$ gives a maximum error equal to 0.3% and refinement along the z-axis gives a maximum error less than 0.03%.

For this study, the critical Grashof number was localized by noting the velocity components and dimensionless temperature at pre-selected points to see if periodic oscillations develop. If, for a Grashof number, no oscillations are detected, its velocity and temperature are

Table 1
Number of mesh points along z, nz, total number of mesh points, N, critical Grashof number for the first steady bifurcation, Gr_{sb}, critical Grashof number for the onset of oscillations, Gr_c, precision δGr_c, and fundamental frequency, f, for aspect ratios $A = 2$ and 3

A	2	3
nz	27	43
N	21 627	34 443
Gr_{sb}	230 000	155 750
Gr_c	234 000	156 500
δGr_c	250	100
f	69.7	5.12

Table 2
Number of mesh points along z, nz, total number of mesh points, N, critical Grashof number for the onset of oscillations, Gr_c, precision δGr_c, and fundamental frequency, f, for aspect ratios $A = 1.5$ and $A \geqslant 4$

A	1.5	4	5	6	7	8	9	10
nz	27	43	49	49	51	55	59	61
N	21 627	34 443	39 249	39 249	40 851	44 055	47 259	48 861
Gr_c	930 000	179 700	275 000	675 000	775 000	925 000	875 000	845 000
δGr_c	5000	100	1000	1000	5000	5000	5000	5000
f	145.7	62.25	101.1	436.7	10.3	2.3	11.4	15.38

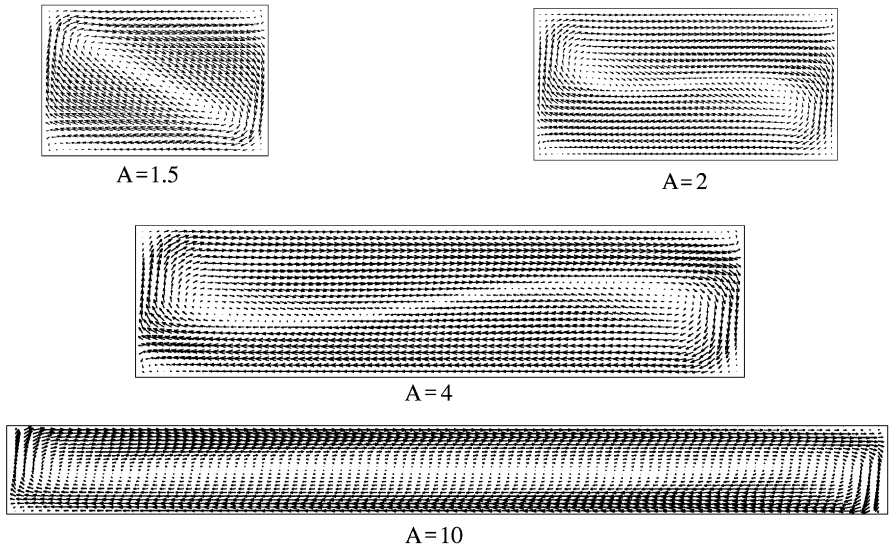

Fig. 2. Velocity fields at steady state in the L_v-plane for $A = 1.5, 2, 4$, and 10, respectively at $Gr = 910\,000$, $220\,000$, $170\,000$, and $750\,000$ ($Pr = 0.026$).

used as initial guesses for the next calculation with an increased Grashof number. This process is repeated until oscillations are detected, and the lowest Grashof number at which oscillations are detected is taken as the critical Grashof number. For some calculations, additional simulations were performed for higher Gr and the amplitudes of the oscillations were noted. Then the value of Gr obtained by extrapolation to zero of the amplitudes was used to accelerate the localization of the transition. Using this procedure, the value of Gr_c was determined with a precision δGr_c (the increment in Grashof number close to the threshold) which is given in Tables 1 and 2 together with the value of Gr_c.

4. Results

In Fig. 2 are shown, for $A = 1.5$, 2, 4, and 10, the plots of the velocity vectors in the L_v-plane for primary steady flows obtained in each case slightly below the first bifurcation. It is clear that, as expected, the steady flows correspond to large convective loops and verify all the original symmetries of the problem. But we notice important changes in the flow structure when A is increased. For $A = 1.5$, the convective loop appears to be strongly tilted inside the cavity, and the limit between the upper and lower reverse flows is almost a straight line close to the second diagonal of the rectangular section. For $A = 2$ and 4, the flow structure appears quite different. The limit between the upper and lower reverse flows has rather a S shape. The flows at both ends of the cavity change their directions but also move towards the axis determining pseudo-recirculations in these end regions inside the convective loop. This phenomenon also induces an interaction between the upper and lower reverse flows around the center of the cavity, in a zone whose extend increases with A. Similar flows are found until $A = 6$. For $A \geqslant 7$, the flows still look different in the L_v-plane with the disappearance of a clear S-shaped limit between the upper and lower reverse flows (see Fig. 2 for $A = 10$). In fact, for these cases, the main flow does not occur in the L_v-plane, but on both sides of this plane, and the end effects do not affect the center part of the cavity.

Concerning the flow transitions, an oscillatory instability develops first for $A = 1.5$ and $A \geqslant 4$. This instability generally breaks the symmetries S_a and S_c except for $A = 1.5$, $A = 6$, and $A = 10$ where none of the symmetries are broken. A different behavior is observed for containers with aspect ratios $A = 2$ and 3: a steady bifurcation occurs first, before oscillatory convection, and breaks the symmetries S_a and S_c. Fig. 3 illustrates this for $A = 2$ by giving

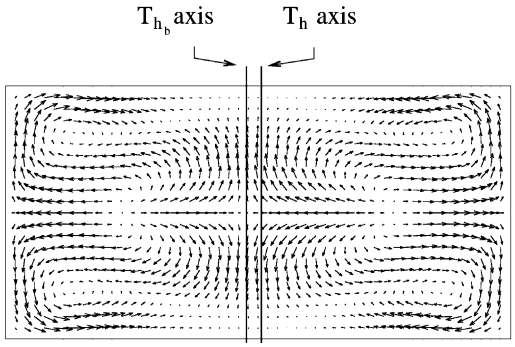

Fig. 3. Velocity field in the L_h-plane for the steady solution obtained beyond a first steady bifurcation for $A = 2$ ($Gr = 230\,000$, $Pr = 0.026$).

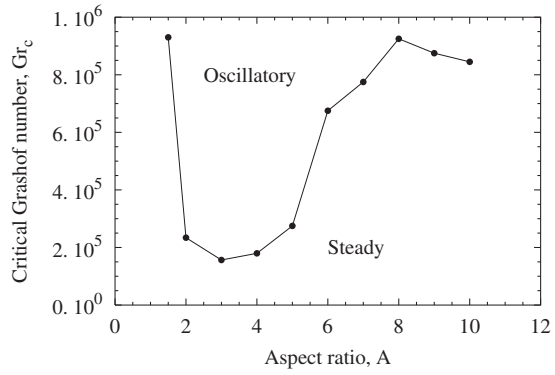

Fig. 4. Evolution of the critical Grashof number for the onset of oscillatory flow, Gr_c, as a function of the aspect ratio A ($Pr = 0.026$).

the new solution beyond the steady bifurcation. The breaking of the symmetry S_a can be viewed as the displacement of the original symmetry axis T_h to a new position T_{h_b}. This steady bifurcation is a supercritical pitchfork bifurcation. This means that another solution, symmetric with respect to S_a of that given in Fig. 3 also exists. With the increase of the Grashof number, a Hopf bifurcation occurs on these new steady branches, but without further loss of symmetry. Note that in all the studied cases, the S_p symmetry is kept at these first transitions.

For $A = 2$ and 3, Table 1 summarizes the values of Gr_{sb} which is the critical Grashof number for the steady bifurcation, those of Gr_c corresponding to the Hopf bifurcation, and the fundamental frequency f of the oscillations. In a similar way, Table 2 exhibits the results for the other aspect ratios ($A = 1.5$ and $4 \leqslant A \leqslant 10$) where only Hopf bifurcation occurs.

Fig. 4 shows the evolution of the critical Grashof number Gr_c for the transition to the oscillatory flow with the aspect ratio A. The thresholds have been found to strongly vary with the aspect ratio A: by increasing A, they first decrease until $A = 3$, increase then until $A = 8$, before decreasing again for larger A. Concerning the frequencies, they also vary significantly with A. Except for $A = 3$, they are relatively strong for small and moderate aspect ratios ($A \leqslant 6$) and weaker for large aspect ratios ($A \geqslant 7$).

5. Energy analyses

Fluctuating energy balances estimated from the numerical results calculated above onset can be used to determine the physical mechanisms responsible for the stabilization or the destabilization of the flow. We consider $u_i = \overline{u}_i + u'_i$, $\theta = \overline{\theta} + \theta'$, where $\overline{u}_i$ and $\overline{\theta}$ are the time averaged quantities for respectively the velocity and the temperature, and u'_i and θ' are the fluctuating quantities. The rate of change of kinetic energy $\partial K/\partial t = \int_\Omega \frac{1}{2}(\partial u_i'^2/\partial t)\,d\Omega$ is obtained by multiplying (2) by u'_i and integrating over the cylinder volume Ω:

$$\frac{\partial K}{\partial t} = \underbrace{\int_\Omega -\sqrt{Gr}\,u'_i u'_j \frac{\partial \overline{u}_i}{\partial x_j}\,d\Omega}_{E_{ks}} + \underbrace{\int_\Omega -\left(\frac{\partial u'_i}{\partial x_j}\right)^2 d\Omega}_{E_{kd}} + \underbrace{\int_\Omega \sqrt{Gr}\,u'_i\theta'\mathbf{e}_y\,d\Omega}_{E_{kb}}, \tag{4}$$

where x_i ($i = 1, 2, 3$) respectively refer to x, y and z. In a similar way, by multiplying the heat equation (3) by θ' and integrating over Ω, we obtain the rate of change of thermal energy $\partial\Theta/\partial t = \int_\Omega \frac{1}{2}(\partial\theta'^2/\partial t)\,d\Omega$:

$$\frac{\partial \Theta}{\partial t} = \underbrace{\int_\Omega -\sqrt{Gr}\theta' u'_j \frac{\partial \overline{\theta}}{\partial x_j}\,d\Omega}_{E_{ts}} + \underbrace{\int_\Omega -\frac{1}{Pr}\left(\frac{\partial \theta'}{\partial x_j}\right)^2 d\Omega}_{E_{td}}. \tag{5}$$

Note that the rate of change of the total fluctuating kinetic energy, $\partial K/\partial t$, has three terms E_{ks}, E_{kd}, and E_{kb} which are respectively the production by shear of the mean flow, the viscous dissipation and the buoyancy contribution. This last term is found to be dissipative for all studied aspect ratios. The rate of change of the fluctuating thermal energy, $\partial\Theta/\partial t$, has only two terms E_{ts} and E_{td} which are respectively the production by transport of the mean temperature gradients and the dissipation by conduction effects.

As it is clear from Fig. 5 where the behaviors of $\partial K/\partial t$ and $\partial\Theta/\partial t$ are exhibited as a function of time for $A = 4$, the main production of fluctuating energy is due to the hydrodynamic effects. This is found to be valid for all the studied aspect ratios. Therefore, in our analysis of the flow transition, we will only consider the fluctuating kinetic energy equation (4). Moreover, as all the signals are time periodic, we will define averaged values over a period and normalize them by the averaged total energy production due to shear $I_s = \langle E_{ks} \rangle$. Among the nine contributions of I_s, we note I_i ($i = 1, 2, 3$) the time-averaged contributions connected to the main flow component, $\overline{w}$, and

J_i ($i = 1, 2, 3$) the corresponding normalized component:

$$J_i = \frac{I_i}{I_s} = \frac{\left\langle \int_\Omega -\sqrt{Gr} u_i' w' \dfrac{\partial \overline{w}}{\partial x_i} \, d\Omega \right\rangle}{I_s}. \quad (6)$$

Examination of the values of the different contributions to the fluctuating kinetic energy balance, summarized in Table 3, shows that the destabilizing effect is mainly due to the shear of the mean flow owing to the $\overline{w}$ component, as these terms contribute to the total production for at least 90%, whereas the terms related to the two other components $\overline{u}$ and $\overline{v}$ have relatively weak contributions.

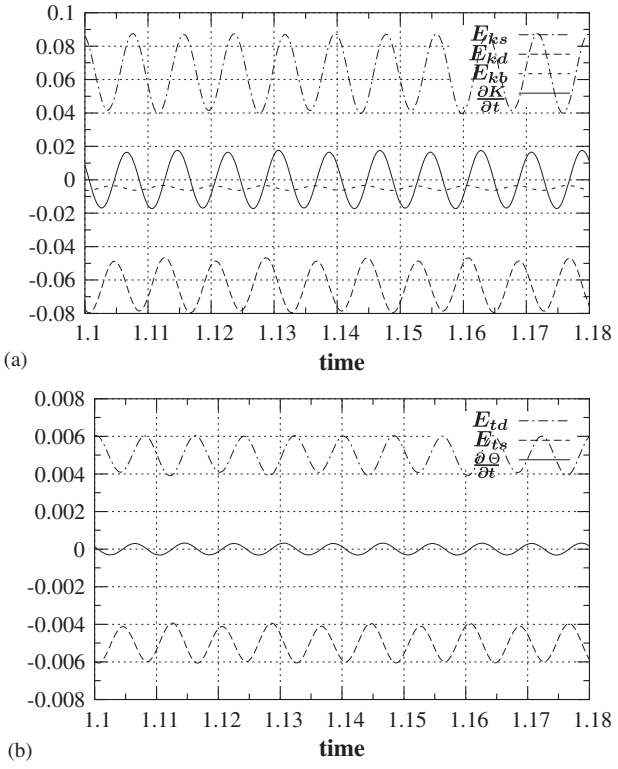

Fig. 5. Time evolutions of the rates of change of the fluctuating kinetic energy $\partial K/\partial t$ (a) and of the fluctuating thermal energy $\partial \Theta/\partial t$ (b), together with their different contributions ($A = 4$, $Gr = 180\,000$, $Pr = 0.026$).

In the same way, we define D_1 and D_2, respectively, for the viscous dissipation term and the buoyancy term:

$$D_1 = \frac{\langle E_{kd} \rangle}{I_s}, \quad D_2 = \frac{\langle E_{kb} \rangle}{I_s}. \quad (7)$$

Note that, close to the threshold, $\langle \partial K/\partial t \rangle$ is negligible so that $-I_s = \langle E_{kd} \rangle + \langle E_{kb} \rangle$ and $D_1 + D_2 = -1$.

According to Table 3, most of the dissipation of the fluctuating kinetic energy is due to the viscous term D_1. However, the buoyancy term D_2 which is rather small, reaches 15% for very small or large aspect ratios corresponding to the largest values of Gr_c. The respective influences of J_1, J_2, and J_3 for the different aspect ratios are rather complex. J_2, related to the vertical gradient of $\overline{w}$, is always destabilizing and it is generally the main destabilizing term, except for $A = 4$ and 5 where it is supplanted by J_3. It is interesting to notice that J_3 can have a stabilizing or destabilizing effect according to the value of the aspect ratio: it was found stabilizing for $A = 1.5, 2, 7$, and 10, and destabilizing for the other studied values of A. As for J_1, it is always destabilizing and its effect is found to be the largest at large aspect ratios ($A \geqslant 7$). If we consider the variations of these quantities in connection with the variations of the thresholds, the main observation is that the steep decrease of the thresholds at small aspect ratios is associated with a large modification of J_3, from a strong stabilizing contribution at $A = 1.5$ to strong destabilizing contributions at $A = 4$ and 5.

In order to better understand the destabilizing mechanisms due to shear, we will decompose the I_i terms into two factors, one connected to the fluctuating fields and the other to the mean flow shear term, and we will quantify their respective influence. In that way, we define spatial contributions averaged over a period, S_{if} and S_{im}, which are such that

$$I_i = \int_\Omega S_i \, d\Omega = \int_\Omega S_{if} S_{im} \, d\Omega \quad \text{with } S_{if} = \langle -\sqrt{Gr} u_i' w' \rangle \quad (8)$$

$$\text{and} \quad S_{im} = \frac{\partial \overline{w}}{\partial x_i}. \quad (9)$$

S_{if} and S_{im} have to be spatially correlated to produce a shear contribution I_i. To characterize this spatial correlation, we have plotted characteristic iso-surfaces close to the extrema values for both S_{if} and S_{im}.

Table 3
Contribution of the terms J_1, J_2, and J_3 to the production of fluctuating kinetic energy through shear effects and contribution of the terms D_1 and D_2 to the dissipation of fluctuating kinetic energy

A	1.5	2	4	5	6	7	8	9	10
J_1	0.173	0.072	0.141	0.105	0.155	0.250	0.289	0.422	0.371
J_2	1.442	0.898	0.346	0.391	0.540	0.713	0.646	0.489	0.671
J_3	−0.715	−0.039	0.484	0.471	0.204	−0.012	0.015	0.020	−0.095
$J_1 + J_2 + J_3$	0.900	0.931	0.972	0.967	0.899	0.950	0.950	0.931	0.946
D_1	−0.843	−0.938	−0.928	−0.938	−0.886	−0.816	−0.812	−0.834	−0.832
D_2	−0.157	−0.062	−0.072	−0.062	−0.114	−0.184	−0.188	−0.166	−0.168

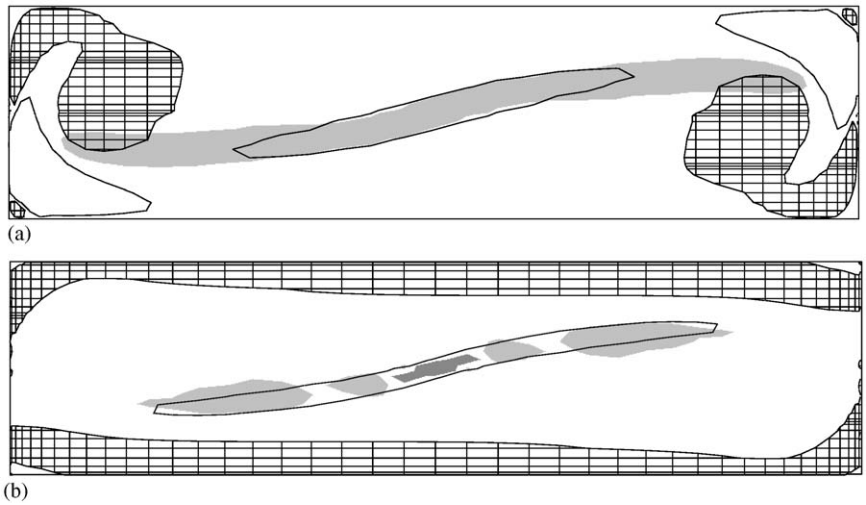

Fig. 6. Section view in the L_v-plane of an iso-surface of S_{3f} (light gray shaded iso-surface for $S_{3f} = -0.102$ (surrounding a minimum value of -1.231)) and iso-surfaces of S_{3m} (empty iso-surface for $S_{3m} = -0.35$ (minimum at -7.83) and meshed iso-surface for $S_{3m} = 0.7$ (maximum at 4.26)) (a). Section view in the L_v-plane of isosurfaces of S_{2f} (light gray shaded iso-surface for $S_{2f} = -0.0397$ (minimum at -0.110) and dark gray shaded iso-surface for $S_{2f} = 0.01$ (maximum at 0.103)) and isosurfaces of S_{2m} (empty iso-surface for $S_{2m} = -7.91$ (minimum at -14.132) and meshed iso-surface for $S_{2m} = 0$ (maximum at 31.525)) (b). The oscillatory case considered here corresponds to $A = 4$, $Gr = 180\,000$, and $Pr = 0.026$.

We first analyze the case $A = 4$ where both I_2 and I_3 have strong contributions. For this case, as the destabilizing phenomena principally occur in the L_v-plane, we plot the different quantities in this plane. Fig. 6(a) shows an iso-surface for S_{3f} (light gray shaded iso-surface) and iso-surfaces for S_{3m} (empty or meshed iso-surfaces). We can see that there is a good spatial correlation between negative values of S_{3f} and negative values of S_{3m} around the center of the cavity at the limit between the upper and lower reverse flows. This gives positive values for S_3 in this region which are responsible for the destabilizing effect of I_3. Note that positive values of S_{3m} are found closer to the endwalls which induce a small stabilizing influence.

Concerning I_2, Fig. 6(b) shows positive and negative iso-surfaces for S_{2f} (respectively dark gray and light gray shaded iso-surfaces) and for S_{2m} (respectively meshed and empty iso-surfaces). The product of these two terms produces a small zone of dissipation of the fluctuating kinetic energy near the center of the cavity and larger zones of production at the limit of the upper and lower reverse flows. The global effect corresponds to a destabilizing contribution for I_2.

The importance of the term I_3 for $A = 4$ is first connected to the existence of a negative gradient $\partial\overline{w}/\partial z$ in the center part of the cavity. This gradient results from the interaction of the upper and lower reverse flows in the center part of the cavity (see Fig. 2). Note that such interaction would not exist in the case of a parallel flow. However, this gradient part in I_3 remaining small compared to the gradient part $(\partial\overline{w}/\partial y)$ in I_2, the preponderance of I_3 over I_2 is connected to the more efficient contribution of the fluctuating part S_{3f} compared to S_{2f}. In fact S_{3f} based on $-w'w'$ has a uniform negative sign, whereas S_{2f} based on $-v'w'$ can have a positive or negative sign. Moreover, the v' fluctuations are small compared to the w' fluctuations.

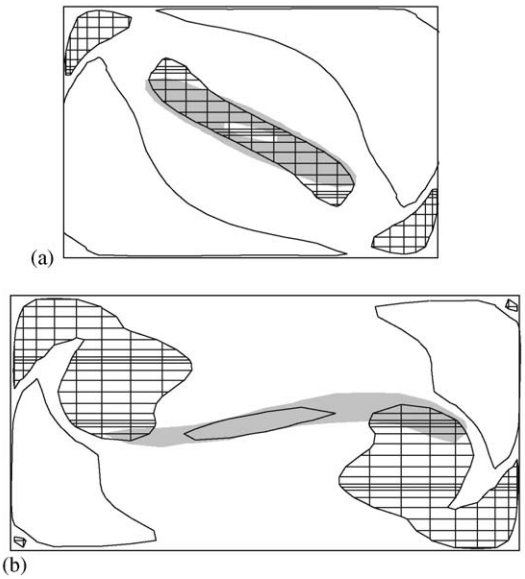

Fig. 7. Section view in the L_v-plane of an iso-surface of S_{3f} (light gray shaded iso-surface for $S_{3f} = -0.369$ (minimum at -1.02)) and iso-surfaces of S_{3m} (empty iso-surface for $S_{3m} = -0.312$ (minimum at -4.921) and meshed iso-surface for $S_{3m} = 1.384$ (maximum at 3.817)) for the oscillatory case $A = 1.5$, $Gr = 930\,000$, and $Pr = 0.026$ (a). Section view in the L_v-plane of an iso-surface of S_{3f} (light gray shaded iso-surface for $S_{3f} = -0.064$ (minimum at -0.771)) and iso-surfaces of S_{3m} (empty iso-surface for $S_{3m} = -0.410$ (minimum at -5.89) and meshed iso-surface for $S_{3m} = 0.757$ (maximum at 3.322)) for the oscillatory case $A = 2$, $Gr = 236\,000$, and $Pr = 0.026$ (b).

It is interesting to consider smaller aspect ratios in order to analyze the strong variation of I_3 occurring in this range of aspect ratio. Results concerning S_{3f} and S_{3m} in the L_v-plane are shown in Fig. 7 for $A = 1.5$ and 2. We see that for

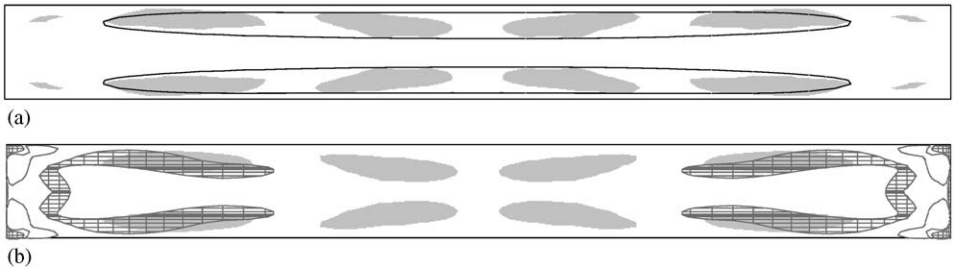

Fig. 8. Section view in the L_h-plane of an iso-surface of S_{2f} (light gray shaded iso-surface for $S_{2f} = -0.001$ (minimum at -0.0084)) and an iso-surface of S_{2m} (empty iso-surface for $S_{2m} = -6.401$ (minimum at -12.857)) (a). Section view in the L_h-plane of an iso-surface of S_{3f} (light gray shaded iso-surface for $S_{3f} = -0.014$ (minimum at -0.0825)) and iso-surfaces of S_{3m} (empty iso-surface for $S_{3m} = -0.586$ (minimum at -6.213) and meshed iso-surface for $S_{3m} = 0.190$ (maximum at 6.38)) (b). The oscillatory case considered here corresponds to $A = 10$, $Gr = 850\,000$, and $Pr = 0.026$.

$A = 1.5$, there is a zone with $\partial\overline{w}/\partial z$ positive in the center of the cavity leading to a strong stabilizing contribution. In fact, for this case, as shown in Fig. 2, the roll is tilted in the cavity, but the flow is almost parallel and there is no interaction between the upper and lower flows in the center of the cavity. For $A = 2$, such interaction exists (Fig. 2) which leads to a zone with $\partial\overline{w}/\partial z$ negative in the center of the cavity (destabilizing influence), but zones with $\partial\overline{w}/\partial z$ positive are also present closer to the endwalls similarly to the case $A = 4$ (stabilizing influence). When the aspect ratio is increased from 2 to 4, the destabilizing zone with $\partial\overline{w}/\partial z$ negative increases in size and this zone becomes large and strongly dominant for $A = 4$ as shown previously in Fig. 6(a). Note that for small aspect ratio, the dominant destabilizing shear term is I_2. As observed for $A = 4$, the zones of production of fluctuating kinetic energy through positive values of S_2 are located along the surface separating the upper and lower reverse flows.

For the intermediate aspect ratios $A = 5$ and 6, we note that the values of I_2 and I_3 are of the same order of magnitude as those obtained for $A = 4$ and the way by which S_2 and S_3 contribute to these terms is also similar to what is observed for $A = 4$.

Concerning long cavities ($A \geqslant 7$) for which I_2 is dominant, the region of main shear stress (negative values of $\partial\overline{w}/\partial y$) is not in the L_v-plane but located on both sides of this plane (empty iso-surface shown in the L_h-plane for $A = 10$ in Fig. 8(a)) inducing a production of fluctuating kinetic energy through S_2 in this region. As for I_3, S_{3m} (empty and meshed iso-surfaces in Fig. 8(b)) is significant only in the end parts of the cavity. Its interaction with S_{3f} (always negative, light gray shaded iso-surfaces in Fig. 8(b)) occurs for $A = 10$ for positive values of S_{3m} (and still outside the L_v-plane), which induces a global stabilizing contribution for I_3 in this case. Finally, the variations of the flow structure in the transverse direction observed for long cavities may explain the significant contributions of I_1 which is connected to shear in this transverse direction.

6. Snapshots

In the previous sections, we have seen that different types of instabilities can be found when varying the aspect ratio.

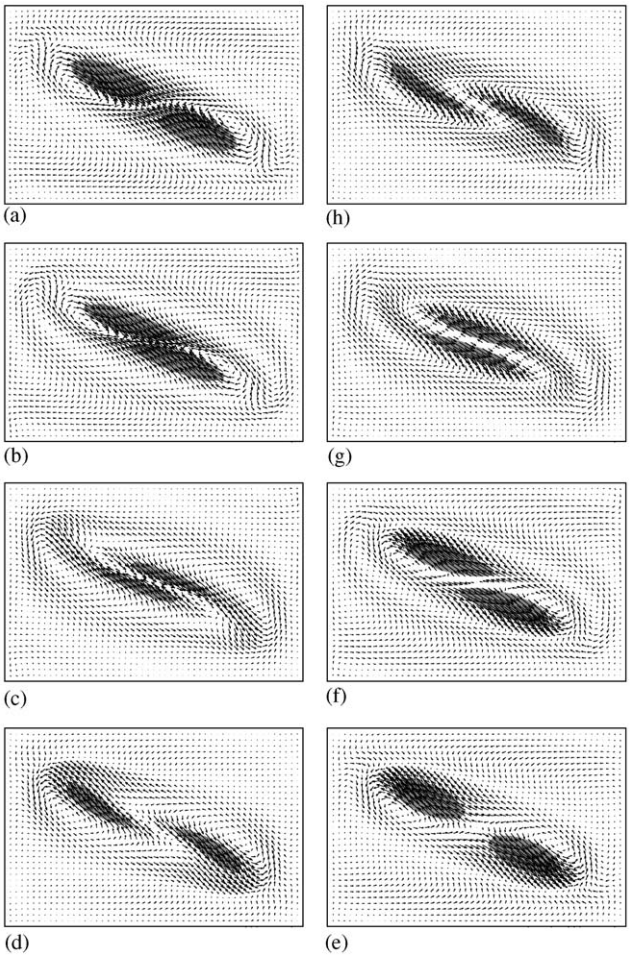

Fig. 9. Fluctuating velocity field and gray patches indicating zones of maximum of fluctuating kinetic energy in the L_v-plane given as a sequence of snapshots over one period of oscillation: (a) $t = 0$, (b) $t = T/8$, (c) $t = 2T/8$, (d) $t = 3T/8$, (e) $t = 4T/8$, (f) $t = 5T/8$, (g) $t = 6T/8$, (h) $t = 7T/8$. The parameters are $A = 1.5$, $Gr = 930\,000$, $Pr = 0.026$.

But, even a detailed consideration of the characteristics involved (sequence of bifurcations, frequencies, symmetry breakings, energy balances) does not allow to clearly and definitively distinguish and localize them. A more powerful stability analysis of these three-dimensional situations would be required. Nevertheless, to get more insight in some of the oscillatory behaviors involved, we will consider

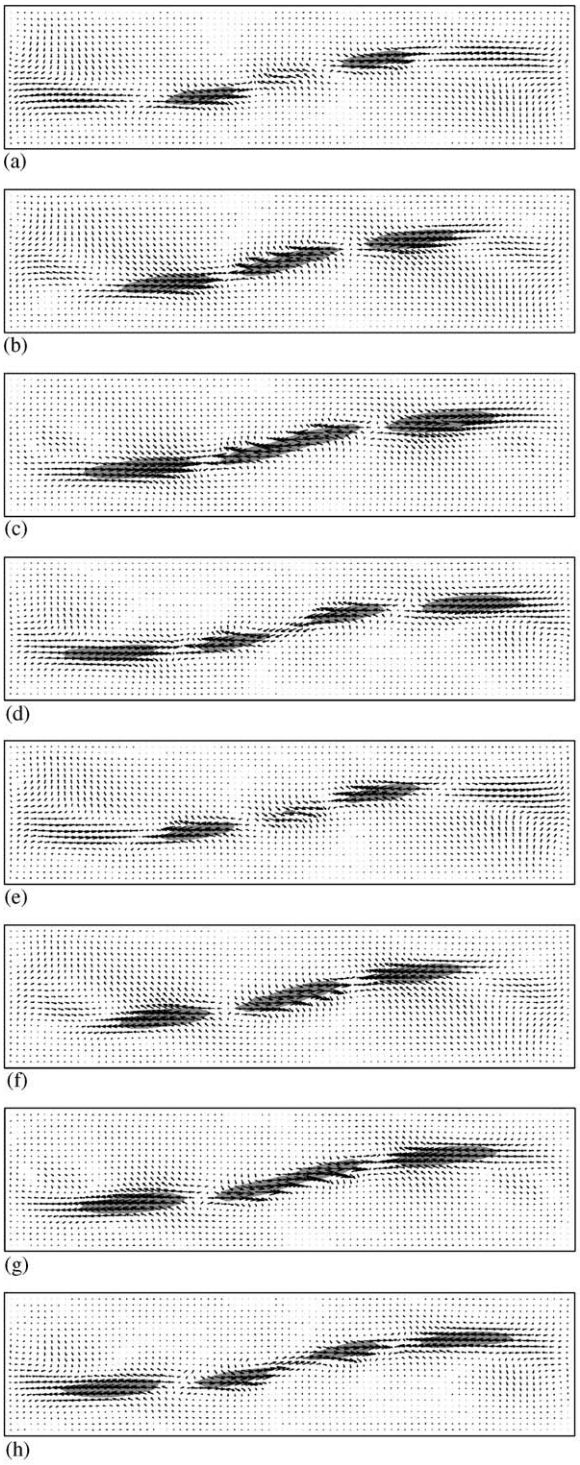

Fig. 10. Sequence of snapshots as in Fig. 9. The parameters are $A = 4$, $Gr = 180\,000$, $Pr = 0.026$.

sequences of snapshots of the fluctuating part of the velocity taken over one period of oscillation. These snapshots are given in the L_v-plane for $A = 1.5$ and 4 (Figs. 9 and 10) and in the L_h-plane for $A = 10$ (Fig. 11) through the projected fluctuating velocity field and gray patches indicating zones of maximum of fluctuating kinetic energy.

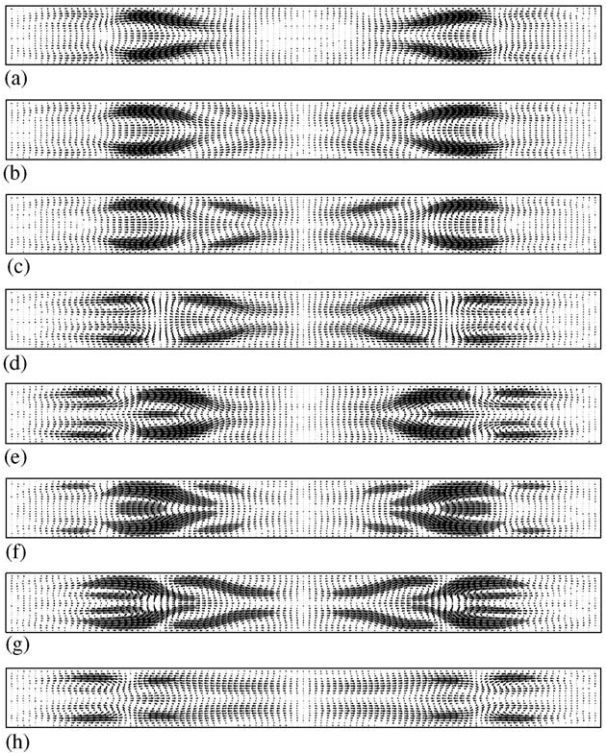

Fig. 11. Sequence of snapshots as in Fig. 9. The parameters are $A = 10$, $Gr = 850\,000$, $Pr = 0.026$.

Different behaviors are found for the three cases considered. For $A = 1.5$ (Fig. 9), the fluctuating field can be viewed as a two-pole structure rotating in the clockwise direction around the center of the cavity. For $A = 4$ (Fig. 10), the fluctuations (anti-symmetric with respect to the center point) seem to originate at this center point, then split into two parts which move towards the ends of the cavity along the line separating the upper and lower reverse flows. Finally, for $A = 10$ (Fig. 11), symmetric fluctuations are generated on both sides of the L_v-plane close to the T_h-axis. These fluctuations move symmetrically towards the ends of the cavity, with an intensity first amplifying and then decaying.

7. Conclusion

At first sight, given that the confinement is lower with the increase of A, we could think that the critical threshold for the onset of oscillations, Gr_c, would decrease in a monotonous way. Our numerical experiments at a Prandtl number 0.026 have established that the thresholds, as well as the fundamental frequencies of the oscillations, do not follow this evolution but strongly vary with the aspect ratio A. By increasing A from $A = 1.5$ to 3, the threshold strongly decreases before strongly increasing until $A = 8$ and finally decreasing for larger A. Moreover, we obtain, for large aspect ratios, a low fundamental frequency compared to the frequency obtained for small and

moderate aspect ratios. These behaviors suggest that the mechanisms of flow transition will depend on the aspect ratio. Fluctuating energy analyses close to the threshold indicate that for small aspect ratios, the instability is due to the vertical shear of horizontal velocity and occurs in the main longitudinal vertical plane in the core of the cavity, along the surface separating the upper and the lower reverse flows. On the other hand, for $A = 4$ and 5, the major destabilizing term is the horizontal shear of horizontal velocity. This reflects the interaction between the reverse flows in the stagnation zone around the center of the cavity. For large aspect ratios, vertical shear has also been found as the main instability factor. In this case, the instability still occurs in these main shear regions, but these regions have moved from the longitudinal vertical plane to symmetric places on both sides of this plane.

These three-dimensional computations were carried out on a IBM-SP3 computer with the support of the Centre Informatique National de l'Enseignement Supérieur (CINES).

References

[1] D.T.J. Hurle, E. Jakeman, C.P. Johnson, J. Fluid Mech. 64 (1974) 565.
[2] S.M. Pimputkar, S. Ostrach, J. Crystal Growth 55 (1981) 614.
[3] M.C. Hung, C.D. Andereck, Notes on Numerical Fluid Mechanics, vol 27, Vieweg, Braunschweig, 1990, pp. 338–343.
[4] J.M. Pratte, J.E. Hart, J. Crystal Growth 102 (1990) 54.
[5] A.E. Gill, J. Fluid Mech. 64 (1974) 577.
[6] J.E. Hart, J. Fluid Mech. 132 (1983) 271.
[7] P. Laure, B. Roux, C.R. Acad. Sci. Paris 305 (1987) 1137.
[8] M. Afrid, A. Zebib, Phys. Fluids A 2 (8) (1990) 1318.
[9] D. Henry, M. Buffat, J. Fluid Mech. 374 (1998) 145.
[10] S. Wakitani, J. Heat Transfer 123 (2001) 77.
[11] G.E. Karniadakis, M. Israeli, S.A. Orszag, J. Comput. Phys. 97 (1991) 414.
[12] R. Touihri, H. Ben Hadid, D. Henry, Phys. Fluids 11 (8) (1999) 2078.